A Unified Gas-Kinetic Scheme for Continuum and Rarefied Flows III: Microflow Simulations

Juan-Chen Huang[1], Kun Xu[2,*] and Pubing Yu[2]

[1] *Department of Merchant Marine, National Taiwan Ocean University,
Keelung 20224, Taiwan.*
[2] *Mathematics Department, Hong Kong University of Science and Technology,
Clear Water Bay, Kowloon, Hong Kong.*

Abstract. Due to the rapid advances in micro-electro-mechanical systems (MEMS), the study of microflows becomes increasingly important. Currently, the molecular-based simulation techniques are the most reliable methods for rarefied flow computation, even though these methods face statistical scattering problem in the low speed limit. With discretized particle velocity space, a unified gas-kinetic scheme (UGKS) for entire Knudsen number flow has been constructed recently for flow computation. Contrary to the particle-based direct simulation Monte Carlo (DSMC) method, the unified scheme is a partial differential equation-based modeling method, where the statistical noise is totally removed. But, the common point between the DSMC and UGKS is that both methods are constructed through direct modeling in the discretized space. Due to the multiscale modeling in the unified method, i.e., the update of both macroscopic flow variables and microscopic gas distribution function, the conventional constraint of time step being less than the particle collision time in many direct Boltzmann solvers is released here. The numerical tests show that the unified scheme is more efficient than the particle-based methods in the low speed rarefied flow computation. The main purpose of the current study is to validate the accuracy of the unified scheme in the capturing of non-equilibrium flow phenomena. In the continuum and free molecular limits, the gas distribution function used in the unified scheme for the flux evaluation at a cell interface goes to the corresponding Navier-Stokes and free molecular solutions. In the transition regime, the DSMC solution will be used for the validation of UGKS results. This study shows that the unified scheme is indeed a reliable and accurate flow solver for low speed non-equilibrium flows. It not only recovers the DSMC results whenever available, but also provides high resolution results in cases where the DSMC can hardly afford the computational cost. In thermal creep flow simulation, surprising solution, such as the gas flowing from hot to cold regions along the wall

---

*Corresponding author. *Email addresses:* `jchuang@mail.ntou.edu.tw` (J.-C. Huang), `makxu@ust.hk` (K. Xu), `mayupb@ust.hk` (P. B. Yu)

surface, is observed for the first time by the unified scheme, which is confirmed later through intensive DSMC computation.

1 Introduction

The flow regimes are characterized by the Knudsen number *Kn*, which is defined as the ratio of molecular mean free path to a characteristic length scale. The continuum regime is in the range of $Kn < 0.001$, followed by the slip regime $0.001 < Kn < 0.1$. The Knudsen number in the transition regime is between 0.1 and 10. Even though it is commonly believed that the Navier-Stokes equations are applicable in the continuum and slip regimes, the validity of these macroscopic description depends on the physical quantities to be evaluated. Even in a fully continuum flow regime, the Navier-Stokes equations cannot be claimed to describe everything properly, where the ghost effect may appear in some cases [25], especially for those related to heat. Simulation of gas flow around microscale structures becomes important with the rapid development of micro-electro-mechanical systems (MEMS) [15]. As the scale of designed devices goes to *µm* and *nm* length scale, the use of the formal description of macroscopic equations becomes problematic. Unfortunately, experimental study of microflow is also difficult due to the small physical dimensions. Therefore, the development of accurate numerical algorithm for microflow simulation will play an important role, especially for non-equilibrium flow with heat transfer. The numerical challenge for flow in microdevices is that the flow transport may cover the whole flow regimes, from continuum to free molecular ones.

The direct simulation Monte Carlo (DSMC) method is a particle-based simulation method for rarefied flows [6, 10]. The validity of this method has been presented in an enormous amount of research papers. Due to the particle based nature, the DSMC method cannot effectively reduce the statistical scattering encountered in microscale flows, which presents a very large noise to information ratio for flows having low speed and/or small temperature variation. Since the statistical scattering inherent in DSMC decreases with the inverse square root of the sample size, an extremely large sample size is required to reduce it to a level that is small in comparison with the small macroscopic velocity. This makes DSMC simulation of MEMS flows extremely time-consuming. Many small temperature variation phenomena can be hardly identified. Even with so many limitations in the DSMC method for the microflow computations, the DSMC method is still a reliable and accurate method here. In order to improve its efficiency, many attempts have been tried. One of the attractive scheme is the information preservation (IP) method for low speed rarefied gas flows [14, 20, 26, 40]. Since IP-DSMC updates the macroscopic variables for each DSMC particle, how to evolve the macroscopic variables when two DSMC particles get collision is still an active research topic. Another promising

approach to improve the efficiency of the DSMC method is the low-noise DSMC through the modeling of linearized Boltzmann equation [11, 22]. In terms of direct kinetic equation solvers, many schemes have been developed [4, 7, 21, 28–30]. In the transport part of these Boltzmann solvers, the collisionless Boltzmann equation is usually used for the flux evaluation, i.e., the so-called Discrete Ordinate Method (DOM). As a result, similar to the DSMC method, the time step in these explicit schemes should be smaller than the particle collision time in order to make the numerical discretization to be consistent with the physical reality. Therefore, great difficulties will be encountered as well in these methods in the low Knudsen number limit, where the cell size may be much larger than the particle mean free path.

In the past decade, without discretizing the particle velocity space many attempts have been made to develop gas-kinetic schemes for the non-equilibrium flow computation [35,38,39]. But, the success is limited. In recent years, based on the Boltzmann-model equations, i.e., the BGK and Shakhov models, with the discretization of particle velocity space we have successfully developed unified schemes for flows in the entire Knudsen number regimes [17, 36, 37]. The unified scheme is a multi-scale method with the update of both macroscopic conservative flow variables and microscopic gas distribution function. The novelty of the approach is the coupled treatment of particle transport and collision in the evaluation of interface fluxes for the update of both macroscopic flow variables and microscopic gas distribution function. The integral solution of the kinetic equation is used to determine the time-dependent gas distribution function at a cell interface. This solution covers flow physics in different scales: the hydrodynamic scale NS distribution function from the integration of the equilibrium state and the kinetic scale free transport mechanism from the initial non-equilibrium gas distribution function. The final determination of the distribution function at a cell interface depends on the ratio between the time step to the local particle collision time. Extensive numerical tests and comparison with DSMC data and experimental measurements have been conducted in the previous studies [13, 17, 32, 36, 37].

The purpose of this paper is to validate the unified scheme for micro-flow computations. The test cases presented are mostly considered as difficult ones in the literature. Traditionally, due to the intrinsic noise in the DSMC solution, in order to speed up the computation some test cases are designed by using an unreasonable assumption in its flow condition, such as a $200K$ temperature jump over a distance of $200nm$. Besides using these cases for validating the unified scheme, we have also tried more practical ones, such as the cases with small temperature variation in the thermal creep flows. The numerical efficiency of the unified scheme does not sensitively depend on the magnitude of temperature variation. But, the smaller the temperature variation is, the more efficient the unified scheme is to get the steady state solution.

This paper is organized as the following. Section 2 is about the introduction of the unified scheme. Section 3 includes tests to demonstrate the performance of the scheme. The last section is the discussion and conclusions.

2   Unified scheme for microflow simulations

Microflows are usually associated with low speed and the flow can cover the whole flow regimes from continuum to free molecular. Due to the low speed, the number of mesh points in the particle velocity space can be much reduced. The numerical experiments in the next section show that a velocity space with 28×28 mesh points in the 2D calculations seems adequate in the transition regime. Here we summarize the unified method.

The two-dimensional gas-kinetic BGK-Shakhov equation can be written as [8, 12, 23]

$$f_t + u f_x + v f_y = \frac{f^+ - f}{\tau}, \tag{2.1}$$

where f is the gas distribution function and f^+ is the heat flux modified equilibrium state which is approached by f,

$$f^+ = g\left[1 + (1 - \mathrm{Pr})\mathbf{c} \cdot \mathbf{q}\left(\frac{c^2}{RT} - 5\right)\Big/(5pRT)\right] = g + g^+,$$

with random velocity $\mathbf{c} = \mathbf{u} - \mathbf{U}$ and the heat flux $\mathbf{q}$. In the above model, the Prandtl number is automatically fixed by choosing the proper value Pr. Both f and f^+ are functions of space (x, y), time t, particle velocity (u, v) in x- and y-directions and the particle velocity w in z-direction. The particle collision time τ is related to the viscosity and heat conduction coefficients, i.e., $\tau = \mu / p$, where μ is the dynamic viscosity coefficient and p is the pressure. In this paper, we only consider monatomic gas in 2D case, the equilibrium Maxwellian distribution is,

$$g = \rho\left(\frac{\lambda}{\pi}\right)^{\frac{3}{2}} e^{-\lambda((u-U)^2 + (v-V)^2 + w^2)},$$

where ρ is the density, (U, V) is the macroscopic velocity in the x and y directions, λ is equal to $m/2kT$, m is the molecular mass, k is the Boltzmann constant and T is the temperature. The relation between mass ρ, momentum $(\rho U, \rho V)$ and energy ρE densities with the distribution function f is

$$\begin{bmatrix} \rho \\ \rho U \\ \rho V \\ \rho E \end{bmatrix} = \int \psi_\alpha f \, d\Xi, \quad \alpha = 1, 2, 3, 4, \tag{2.2}$$

where ψ_α is the component of the vector of moments

$$\boldsymbol{\psi} = (\psi_1, \psi_2, \psi_3, \psi_4)^T = \left(1, u, v, \frac{1}{2}(u^2 + v^2 + w^2)\right)^T,$$

and $d\Xi = du\,dv\,dw$ is the volume element in the phase space. Since mass, momentum and energy are conserved during particle collisions, f and g satisfy the conservation constraint,

$$\int (g - f)\psi_\alpha \, d\Xi = 0, \quad \alpha = 1, 2, 3, 4, \tag{2.3}$$

at any point in space and time.

The unified scheme is a finite volume method. The physical space is divided into control volume, i.e., $\Omega_{i,j} = \Delta x \Delta y$ with the cell sizes Δx and Δy in the rectangular case. The temporal discretization is denoted by t^n for the n_{th} time step. The particle velocity space is discretized by a rectangular mesh points with velocity spacing Δu and Δv, with the center of the (k,l)-velocity interval at $(u_k, v_l) = (k\Delta u, l\Delta v)$. The averaged gas distribution function in a physical control volume $\Omega_{i,j}$, at time t^n and around particle velocity (u_k, v_l), is given by

$$f(x_i, y_j, t^n, u_k, v_l) = f^n_{i,j,k,l} = \frac{1}{\Delta x \Delta y \Delta u \Delta v} \iint_{\Omega_{i,j}} \iint_{\Delta u \Delta v} \int_{-\infty}^{+\infty} f(x, y, t^n, u, v, w) dx dy d\Xi. \quad (2.4)$$

The kinetic BGK-Shakhov equation (2.1) can be written as

$$f_t = -u f_x - v f_y + \frac{f^+ - f}{\tau}. \quad (2.5)$$

Integrating the above equation in a physical control volume and keeping the particle velocity space continuous, the above differential equation becomes an integral equation

$$f^{n+1}_{i,j} = f^n_{i,j} + \frac{1}{\Omega_{i,j}} \int_{t^n}^{t^{n+1}} \sum_{m=1}^{m=n} u_m \hat{f}_m(t) \Delta S_m dt + \frac{1}{\Omega_{i,j}} \int_{t^n}^{t^{n+1}} \iint_{\Omega_{i,j}} \frac{f^+ - f}{\tau} d\Omega dt, \quad (2.6)$$

where $\hat{f}_m$ is the gas distribution function at a cell boundary, n is the total number of piecewise linear interfaces of a control volume $\Omega_{i,j}$, u_m is the particle velocity normal to the cell interface and ΔS_m is the m-th interface length. Actually, Eq. (2.6) can be considered as a direct flow modeling in a control volume and the volume integration of the source term can be written generally as an integration of a reasonable particle collision term Q, such as the BGK, Shakhov, ES-BGK, or even full Boltzmann model. Physically, Eq. (2.6) is more fundamental than Eq. (2.5), because it can be derived directly by physical modeling on a realistic numerical framework with limited cell size and time step. If we consider Eq. (2.6) as a direct modeling and think of how to get a time-dependent gas distribution function at a cell interface, we can understand why we call the unified scheme as a PDE-based modeling method, because we use the PDE to construct such an evolution solution around the cell interface. And this PDE's evolution solution can be valid over a large time scale, such as to the hydrodynamic time scale, rather than being confined to the kinetic time scale of the equation, such as the particle collision time. If we consider Eq. (2.5) as the fundamental equation, it will not be surprising that we can easily take an inappropriate numerical approximation, such as using the collisionless Boltzmann solution to get the interface distribution function through the so-called upwinding approximation for the transport part.

Taking conservative moments ψ_α on Eq. (2.6), due to the conservation of conservative variables during particle collision process, the update of conservative variables becomes

$$W^{n+1}_{i,j} = W^n_{i,j} + \frac{1}{\Omega_{i,j}} \int_{t^n}^{t^{n+1}} \sum_{m=1}^{m=n} \Delta \mathbf{S}_m \cdot \mathbf{F}_m(t)) dt, \quad (2.7)$$

where W is the cell averaged conservative mass, momentum and energy densities inside each control volume and **F** is the fluxes of the macroscopic flow variables across the cell interface. This flux will be calculated through the local solution of the kinetic equation.

The critical step for the unified scheme is to evaluate a time-dependent gas distribution function at a cell interface. In a local coordinate system with the x-direction as the normal one, the distribution function from the kinetic equation at a cell interface can be written as [18,34],

$$
\begin{aligned}
\hat{f}_{j+1/2,k,l} &= f(x_{j+1/2},t,u_k,v_l,w) \\
&= \frac{1}{\tau}\int_{t^n}^{t^{n+1}} f^+(x',t',u_k,v_l,w)e^{-(t-t')/\tau}dt' \\
&\quad + e^{-(t-t^n)/\tau}f_{0,k,l}^n(x_{j+1/2}-u_k(t-t^n),t^n,u_k,v_l,w),
\end{aligned}
\tag{2.8}
$$

where $f^+ = g+g^+$ will be approximated separately. Here $x' = x_{j+1/2}-u_k(t-t')$ is the particle trajectory and $f_{0,k,l}^n$ is the initial gas distribution function of f at time $t=t^n$ around the cell interface $x_{j+1/2}$ at the particle velocity (u_k,v_l), i.e., $f_{0,k,l}^n = f_0^n(x,t^n,u_k,v_l,w)$. Even the integral solution of the kinetic equation is exact, but it still needs modeling to determine each term in the integral solution, especially in the case with discontinuous initial data.

The above integral equation covers flow physics in many scales. The initial term f_0 accounts for the free transport mechanism along particle trajectory, which represents the kinetic scale physics. The integration of the equilibrium state along the particle path represents the accumulating effect of a Maxwellian, which is related to the hydrodynamic scale flow physics. The integration of the Maxwellian actually presents a NS distribution function. The flow behavior here at the cell interface depends on the ratio of time step and local particle collision time. It covers all flow regimes from free molecular transport to the NS solution. If a Chapman-Enskog expansion is used for the reconstruction of the initial gas distribution function f_0, the corresponding scheme for the update macroscopic variables in Eq. (2.7) is the gas-kinetic BGK-NS method for the NS solutions [34]. However, for the unified scheme, the gas distribution function itself is updated and $f_{0,k,l}^n$ is known at the beginning of each time step t^n. Therefore, a high-order reconstruction scheme can be used directly to obtain its subcell solution of f_0 without using Chapman-Enskog expansion. In this aspect, the unified scheme does not require any knowledge of the kinetic theory, such as the Chapman-Enskog expansion. For most other DOM methods, instead of using the integral solution for the interface gas distribution function, only f_0 is used for the flux evaluation. Therefore, it will mis-interpret the flow physics in the continuum flow regime, except the mesh size is smaller than the particle mean free path and the time step is less than the particle collision time.

Around each cell interface $x_{j+1/2}$, at time step t^n the initial distribution function becomes,

$$
f_0(x,t^n,u_k,v_l,w) = f_{0,k,l}(x,0) = \begin{cases} f_{j+1/2,k,l}^L + \sigma_{j,k,l}x, & x \leq 0, \\ f_{j+1/2,k,l}^R + \sigma_{j+1,k,l}x, & x > 0, \end{cases}
\tag{2.9}
$$

where nonlinear limiter is used to obtain $f^L_{j+1/2,k,l}$, $f^R_{j+1/2,k,l}$ and the corresponding slopes $\sigma_{j,k,l}$, $\sigma_{j+1,k,l}$. The van Leer limiter will be used in the reconstruction.

There is one-to-one correspondence between an equilibrium state and macroscopic flow variables. For an equilibrium state g around a cell interface $(x_{j+1/2}=0,t=0)$, it can be expanded with two slopes [34],

$$g=g_0\left[1+(1-H[x])\bar{a}^L x+H[x]\bar{a}^R x+\bar{A}t\right],\tag{2.10}$$

where $H[x]$ is the Heaviside function defined as

$$H[x]=\left\{\begin{array}{ll} 0, & x<0, \\ 1, & x\geq0. \end{array}\right.$$

Here g_0 is a local Maxwellian distribution function located at $x=0$. Even though, g is continuous at $x=0$, but it has different slopes at $x<0$ and $x\geq0$. In the equilibrium state g, $\bar{a}^L$, $\bar{a}^R$ and $\bar{A}$ are related to the derivatives of a Maxwellian distribution in space and time.

The determination of g_0 depends on the determination of the local macroscopic values of ρ_0, U_0, V_0 and λ_0 in g_0, i.e.,

$$g_0=\rho_0\left(\frac{\lambda_0}{\pi}\right)^{\frac{3}{2}}e^{-\lambda_0((u-U_0)^2+(v-V_0)^2+w^2)},$$

which is determined uniquely using the compatibility condition of the BGK model. The conservation constraint at $(x=x_{i+1/2},t=0)$ gives

$$W_0=\int g_0\boldsymbol{\psi}d\Xi=\sum\left(f^L_{i+1/2,k,l}H[u_k]+f^R_{i+1/2,k,l}(1-H[u_k])\right)\boldsymbol{\psi},\tag{2.11}$$

where $W_0=(\rho_0,\rho_0U_0,\rho_0V_0,\rho E_0)^T$ is the conservative macroscopic flow variables located at the cell interface at time $t=0$. Since $f^L_{i+1/2,k,l}$ and $f^R_{i+1/2,k,l}$ have been obtained earlier in the initial distribution function f_0 around a cell interface, the above moments can be evaluated explicitly. Therefore, the conservative variables ρ_0, ρ_0U_0, ρ_0V_0 and ρ_0E_0 at the cell interface can be obtained, from which g_0 is uniquely determined. Based on the same distribution functions $f^L_{i+1/2,k,l}$ and $f^R_{i+1/2,k,l}$, the corresponding heat flux q at the cell interface can be also evaluated according to the definition

$$q=\frac{1}{2}\int(u-U_0)((u-U_0)^2+(v-V_0)^2+w^2)\left(f^L_{i+1/2,k,l}H[u_k]+f^R_{i+1/2,k,l}(1-H[u_k])\right)d\Xi,$$

where the above integration can be replaced by summation over the discrete particle velocity. For the equilibrium state, λ_0 in g_0 can be found from

$$\lambda_0=3\rho_0\Big/\left(4\left(\rho_0E_0-\frac{1}{2}\rho_0(U_0^2+V_0^2)\right)\right).$$

Then, $\bar{a}^L$ and $\bar{a}^R$ of g in Eq. (2.10) can be obtained through the relation of

$$\frac{\bar{W}_{j+1}(x_{j+1})-W_0}{\rho_0\Delta x^+}=\frac{1}{\rho_0}\int \bar{a}^R g_0\psi d\Xi=\bar{M}^0_{\alpha\beta}\begin{bmatrix}\bar{a}^R_1\\\bar{a}^R_2\\\bar{a}^R_3\\\bar{a}^R_4\end{bmatrix}=\bar{M}^0_{\alpha\beta}\bar{a}^R_\beta,$$

$$\frac{W_0-\bar{W}_j(x_j)}{\rho_0\Delta x^-}=\frac{1}{\rho_0}\int \bar{a}^L g_0\psi d\Xi=\bar{M}^0_{\alpha\beta}\begin{bmatrix}\bar{a}^L_1\\\bar{a}^L_2\\\bar{a}^L_3\\\bar{a}^L_4\end{bmatrix}=\bar{M}^0_{\alpha\beta}\bar{a}^L_\beta,$$

where the matrix $\bar{M}^0_{\alpha\beta}=\int g_0\psi_\alpha\psi_\beta d\Xi/\rho_0$ is known, and $\Delta x^+=x_{i+1}-x_{i+1/2}$ and $\Delta x^-=x_{i+1/2}-x_i$ are the distances from the cell interface to cell centers. Therefore, $(\bar{a}^R_1,\bar{a}^R_2,\bar{a}^R_3,\bar{a}^R_4)^T$ and $(\bar{a}^L_1,\bar{a}^L_2,\bar{a}^L_3,\bar{a}^L_4)^T$ can be found following the procedure as BGK-NS method [34]. In order to evaluate the time evolution part $\bar{A}$ in the equilibrium state, we can apply the following condition

$$\frac{d}{dt}\int (g-\hat{f})\psi d\Xi=0,$$

at $(x=0,t=0)$ and get

$$\bar{M}^0_{\alpha\beta}\bar{A}_\beta=\frac{1}{\rho_0}(\partial\rho/\partial t,\partial(\rho U)/\partial t,\partial(\rho V)/\partial t,\partial(\rho E)/\partial t)^T$$

$$=-\frac{1}{\rho_0}\int\left[u\left(\bar{a}^L \mathrm{H}[u]+\bar{a}^R(1-\mathrm{H}[u])\right)g_0\right]\psi d\Xi.$$

With the determination of equilibrium state and the heat flux at the cell interface, the additional term g^+ in the Shakhov model can be well-determined as well.

In the above calculation of the equilibrium state in space and time, it is not necessary to use a discretized particle velocity space. Based on the macroscopic flow distributions, we can construct the integral solution in a continuous particle velocity space first, then take its corresponding value at the specific particle velocity when necessary. After substituting Eq. (2.9) and Eq. (2.10) into Eq. (2.8) and taking $(u=u_k,v=v_l)$ in g_0, $\bar{a}^L$, $\bar{a}^R$ and $\bar{A}$, the gas distribution function $\hat{f}(x_{j+1/2},t,u_k,v_l,w)$ at the discretized particle velocity (u_k,v_l) can be expressed as

$$\hat{f}_{j+1/2,k,l}(x_{j+1/2},t,u_k,v_l,w)$$

$$=(1-e^{-t/\tau})(g_0+g^+)+\left(\tau(-1+e^{-t/\tau})+te^{-t/\tau}\right)\left(\bar{a}^L\mathrm{H}[u_k]+\bar{a}^R(1-\mathrm{H}[u_k])\right)u_k g_0$$

$$+\tau(t/\tau-1+e^{-t/\tau})\bar{A}g_0+e^{-t/\tau}\left((f^L_{j+1/2,k}-u_k t\sigma_{j,k})\mathrm{H}[u_k]\right.$$

$$\left.+(f^R_{j+1/2,k}-u_k t\sigma_{j+1,k})(1-\mathrm{H}[u_k])\right)$$

$$\triangleq \tilde{g}_{j+1/2,k,l} + \tilde{f}_{j+1/2,k,l}, \tag{2.12}$$

where $\tilde{g}_{j+1/2,k,l}$ includes all terms related to the integration of the equilibrium state g and g^+ and $\tilde{f}_{j+1/2,k,l}$ is the terms from initial condition f_0. The collision time τ in the above distribution function is determined by $\tau = \mu(T_0)/p_0$, where T_0 is the temperature and p_0 is the pressure.

In order to discretize the collision term in Eq. (2.6) efficiently, the unified scheme will update the macroscopic variables first through Eq. (2.7), where the flux **F** is evaluated as

$$\mathbf{F} = \int u\psi \hat{f}_{j+1/2,k,l} d\Xi.$$

In the continuum flow region, due to sufficient number of particle collisions and with the condition of time step being much larger than the particle collision time, the contribution of the integration of the equilibrium state $\tilde{g}_{j+1/2}$ will be dominant in the final solution of the distribution function $\hat{f}_{j+1/2,k,l}$. The $\tilde{g}_{j+1/2}$ itself gives a corresponding NS distribution function [33] and the contribution from initial term $\tilde{f}_{j+1/2,k,l}$ vanishes. In the highly non-equilibrium flow regime, Eq. (2.7) for the update of conservative variables is correct as well. For example, in the collisionless limit, the non-equilibrium part $\tilde{f}_{j-1/2,k,l}$ will take dominant effect and the contribution from the equilibrium part vanishes. Therefore, the unified scheme has the correct collision-less limit. The final solution to be obtained in the unified scheme depends on the ratio of t/τ locally. In order words, it depends on the relative mesh size with respect to the local particle mean free path. For example, in the nozzle gas exhausting into vacuum case with density ratio 10^4 [13], inside the nozzle the time step is much larger than the local particle collision time and outside the nozzle the time step is less than the local particle collision time. Therefore, the scheme can capture flow physics in different regions, i.e., the pressure wave inside the nozzle and particle free transport outside.

With the trapezoidal rule for the evaluation of particle collision term inside each control volume, the unified scheme for the update of gas distribution function is

$$f_{i,j,k,l}^{n+1} = \left(1 + \frac{\Delta t}{2\tau_{i,j}^{n+1}}\right)^{-1} \left[f_{i,j,k,l}^n + \frac{1}{\Omega_{i,j}} \int_{t^n}^{t^{n+1}} \sum_m \Delta S_m u_m \hat{f}_{m,k,l} dt \right.$$
$$\left. + \frac{\Delta t}{2} \left(\frac{f^{+(n+1)}_{i,j,k,l}}{\tau_{i,j}^{n+1}} + \frac{f^{+(n)}_{i,j,k,l} - f_{i,j,k,l}^n}{\tau_{i,j}^n} \right) \right], \tag{2.13}$$

where no iteration is needed for the update of the above solution. The particle collision times $\tau_{i,j}^n$ and $\tau_{i,j}^{n+1}$ are defined based on the temperature and pressure in the cell, i.e., $\tau_{i,j}^n = \mu(T_{i,j}^n)/p_{i,j}^n$ and $\tau_{i,j}^{n+1} = \mu(T_{i,j}^{n+1})/p_{i,j}^{n+1}$, which are known due to the updated macroscopic flow variables in Eq. (2.7) at the next time level.

The following is the boundary treatment for the unified scheme, specifically for the microflow at the solid boundary. Suppose that we have a solid wall at the left side, the

incoming gas is moving to the left and impinging on the wall. In all simulations in the next section, the Maxwellian boundary treatment with accommodation coefficient 1 is implemented. Assume that the Maxwellian distribution at the wall is set to be

$$g_w = \rho \left(\frac{\lambda_w}{\pi} \right)^{\frac{3}{2}} \exp \left(-\lambda_w (u^2 + v^2 + w^2) \right), \quad u > 0, \tag{2.14}$$

where $\lambda_w = m/2kT_w$ and the density in the above Maxwellian for the outgoing gas is determined by

$$\int_{t^n}^{t^{n+1}} \int_{u>0} ug_w dudvdwdt + \int_{t^n}^{t^{n+1}} \int_{u<0} uf_{in} dudvdwdt = 0, \tag{2.15}$$

where f_{in} is the distribution function of particles impinging on the wall. Then, the final gas distribution function on the surface of the wall becomes

$$f_w = f_{in}(1 - H(u)) + g_w H(u),$$

which can be used to evaluate the fluxes across the solid boundary. For example, for the update of macroscopic flow variables, the fluxes across the wall can be calculated as

$$\mathbf{F} = \begin{pmatrix} F_\rho \\ F_{\rho U} \\ F_{\rho V} \\ F_{\rho E} \end{pmatrix} = \int_{u>0} ug_w \psi dudvdw + \int_{u<0} uf_{in} \psi dudvdw. \tag{2.16}$$

3   Low speed microflow simulations

3.1   Couette flow

The Couette flow is a steady flow that is driven by the surface shear stresses of two infinite and parallel plates moving oppositely along their own planes [14]. The Knudsen number is defined as $Kn = \lambda_{HS}/h$, where λ_{HS} is the mean free path and h is the distance between the plates.

In the transition regime, three Knudsen numbers are considered: $0.2/\sqrt{\pi}$, $2/\sqrt{\pi}$ and $20/\sqrt{\pi}$. To resolve the flow fields well, 100 cells are employed in the current calculation for all the three cases. Fig. 1(a) compares the velocity profiles given by the unified scheme, the linearized Boltzmann equation [25] and IP-DSMC results [14]. The unified solution has excellent agreement with others. Fig. 1(b) also compares the relation of the surface shear stress versus the Knudsen number given by various methods. The normalization factor is the collisionless solution [14]. The unified solution agrees nicely with linearized Boltzmann solution in the whole flow regimes.

Simple heat conduction problem in rarefied gas is also a valuable case to test the capability to capture thermal effect. This consists of two stationary parallel surfaces maintained at different temperatures. The set up of the problem and the parameters adopted

(a) $Kn = 0.2/\sqrt{\pi}, 2/\sqrt{\pi}, 20/\sqrt{\pi}$ (b) Stress
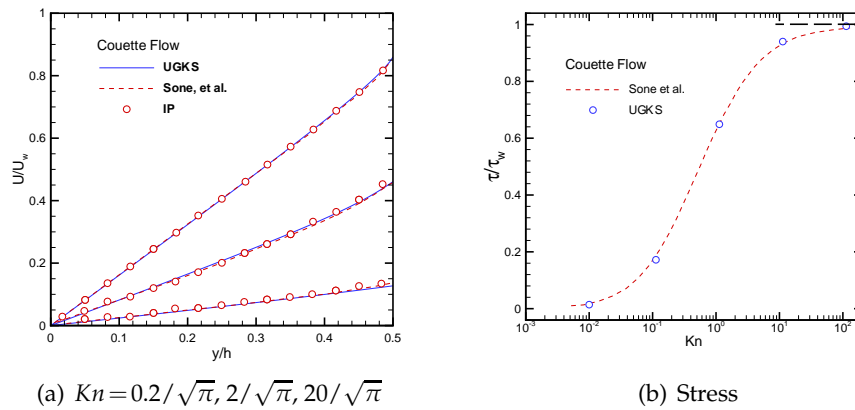
Figure 1: Couette flow. (a) Comparison of velocity profiles in the upper half channel given by the IP method [14], linearized Boltzmann equation [25] and unified Scheme. (b) Relation of drag versus Knudsen number.

(a) Temperature profiles   (b) Heat transfer profiles
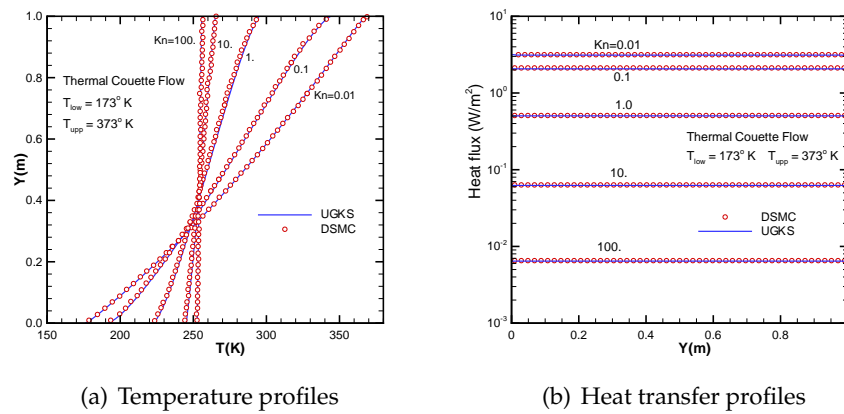
Figure 2: Thermal Couette flow at $Kn = 0.01, 0.1, 1, 10$ and 100 calculated by DSMC and unified scheme.

correspond to those used to test the IP-DSMC method [20,26]. The up and down surfaces are maintained at temperature of 173K and 373K separately with a 1m gap between them and the intervening space is filled with argon gas at various densities to have the corresponding Knudsen numbers $Kn = 0.01, 0.1, 1, 10$ and 100. The 1D computational domain is discretized with 100 cells in the physical space and 28×28 grid points in the velocity space. Fig. 2 presents the temperature profiles and heat flux results from the unified scheme and the benchmark DSMC solution. In comparison with IP-DSMC method, the unified scheme seems get accurate solutions in the rarefied regimes, such as the capturing of heat flux at $Kn = 100$.

3.2 Rayleigh flow

The Rayleigh flow is an unsteady flow in which a plate below a gas at rest suddenly acquires a constant parallel velocity and a constant temperature. The set up of this test

(a) $t = 0.1\tau$

(b) $t = 1\tau$

(c) $t = 10\tau$

(d) $t = 100\tau$
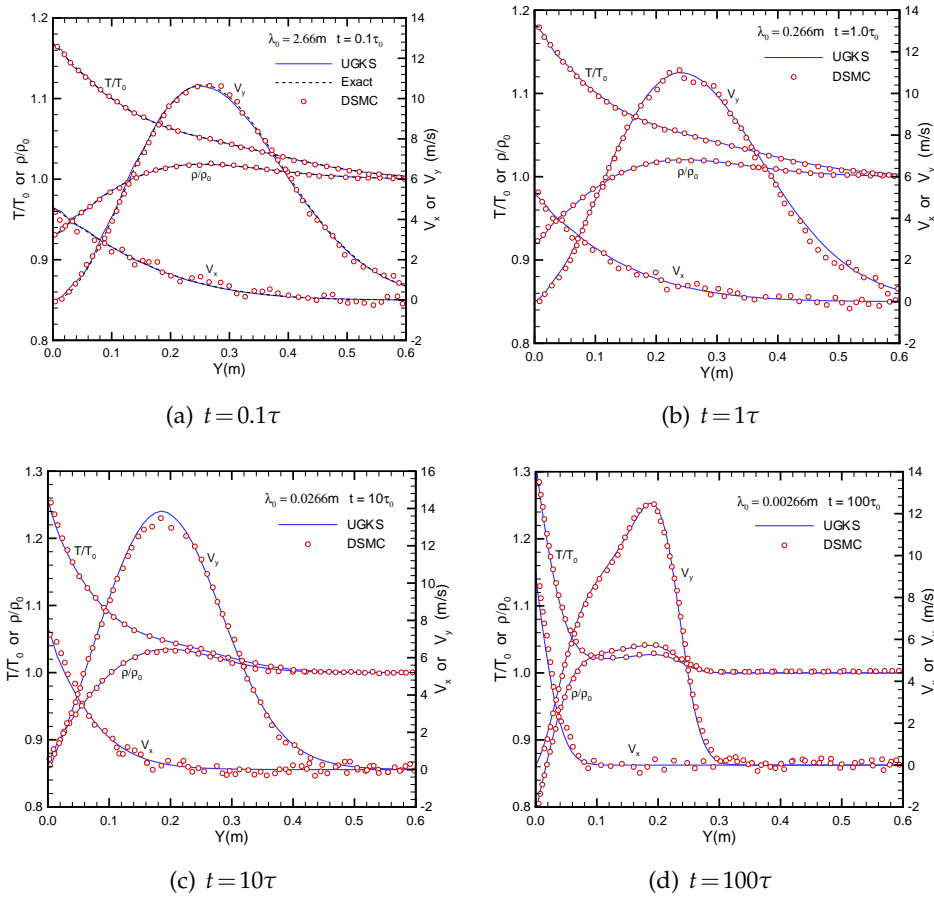
Figure 3: Rayleigh problem at times $t = 0.1\tau, \tau, 10\tau$ and 100τ, which cover the free molecular, transition and continuum regimes. The exact solution at 0.1τ means the solution from collisionless Boltzmann equation.

follows the work by Sun [27]. The initial argon gas is at rest with a temperature of $273K$. When $t > 0$, the plate obtains a constant velocity $10m/s$ and a constant temperature $373K$. There is an analytical solution to the Rayleigh flow for times much less than the mean collision time $\tau_0 = \lambda_m / \nu_m$, where λ_m is the particle mean free path and ν_m is the mean molecular speed with $\nu_m = \sqrt{8RT/\pi}$ [10]. Fig. 3(a) shows the simulated results at $0.1\tau_0$ from the unified scheme and the DSMC solution along with the analytical solution of the collisionless Boltzmann equation at early times. All three solutions agree with each other very well. In comparison with DSMC method, the unified scheme has no statistical scattering in the velocity V_x profile. At time $t = 0.1\tau_0$, the unified scheme recovers the exact collisionless Boltzmann solution. As the time increases to $t = 1\tau_0$ and $10\tau_0$ in the transition regime, the unified solutions and the DSMC solutions are shown in Figs. 3(b) and (c). The small wiggles in V_x and V_y of the DSMC solution are absent in the unified results. The largest discrepancy appears in the peak V_y value at $t = 10\tau_0$. This discrepancy is most

likely due to the low resolution in the DSMC solution. As time goes to $t = 100\tau_0$, the flow goes to the continuum flow regime. Fig. 3(d) presents the results from the unified scheme and the DSMC method. Continuing in this limit, the unified scheme will recover the Navier-Stokes solution accurately. The excellent agreement between unified and DSMC solutions validates the unified scheme in the unsteady flow computation, at least in this simple case.

The main difference between the unified scheme and the traditional DOM method is due to the different ways to evaluate the cell interface flux. For the unified scheme, the integral solution (2.8) is used for the determination of the interface gas distribution function, which covers both hydrodynamic and kinetic scales gas evolution physics. For the DOM methods, only the f_0 term in (2.8) is kept, such as using the collisionless Boltzmann solution for the interface flux. As a result, the DOM methods lack the flow mechanism in the hydrodynamic scale and will have problem in cases where the numerical cell size is much larger than the particle mean free path. For the same Rayleigh problem, as time increases, the wave starting from the wall will propagate upward into a large domain.

(a) $t = 100\tau$

(b) $t = 100\tau$

(c) $t = 200\tau$
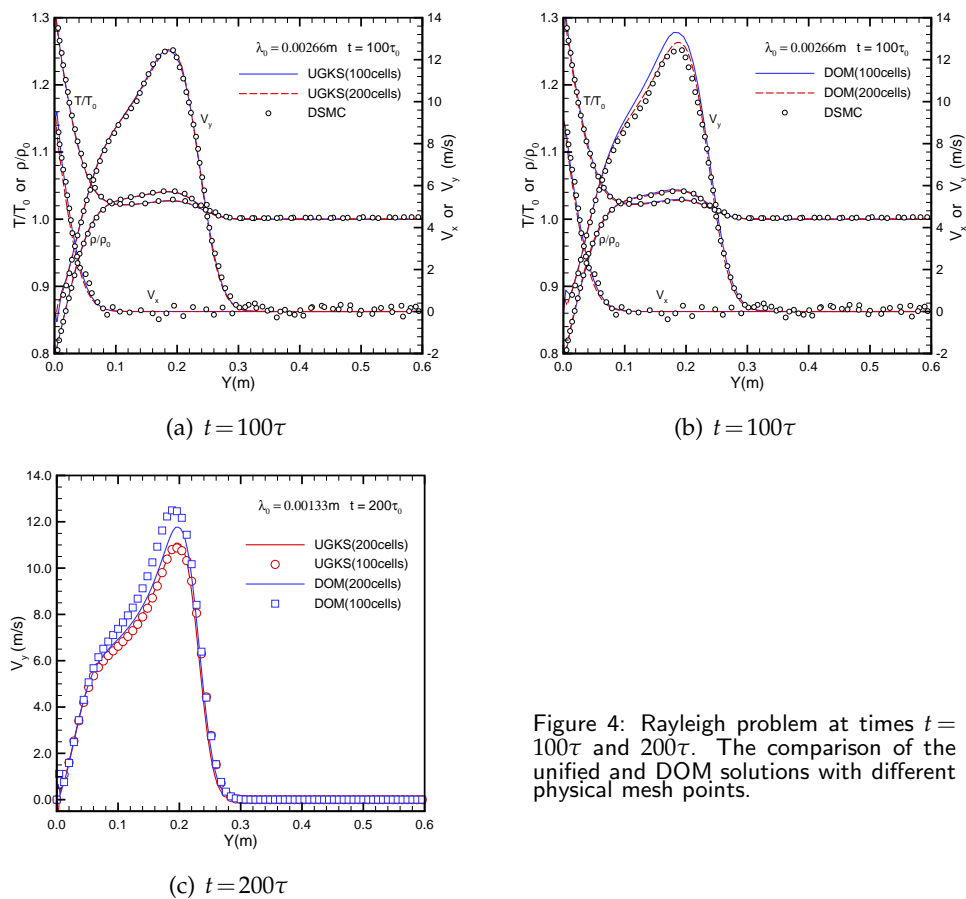
Figure 4: Rayleigh problem at times $t = 100\tau$ and 200τ. The comparison of the unified and DOM solutions with different physical mesh points.

With the same number of cells to resolve the flow in a large domain, such as 100 or 200 cells, the ratio of the cell size over the particle mean free path will become large. Then, the hydrodynamic effect will gradually become important. So, there will have deviation between the solutions of the unified scheme and the DOM method. Figs. 4(a) and (b) present the solutions of the unified and DOM at $t=100\tau$ with 100 and 200 physical mesh points. It is clear that the numerical solution of DOM depends sensitively on the mesh size, but the unified scheme gives the same result even with the change of the ratio of the cell size over particle mean free path. When time goes to 200τ, the difference between unified and DOM solutions becomes more obvious, see Fig. 4(c). Therefore, if we go further into the continuum flow regime, the DOM method will not properly recover the NS solutions when the mesh size is hundreds even thousands of the particle mean free path. Fortunately, for the unified scheme there is no hybrid technique needed to simulate flows with both continuum and rarefied regions.

3.3   Response of a gas to a spatially varying boundary temperature

We simulate the response of argon gas to a boundary temperature with a sinusoidal spatial variation [22]. Here, the lower boundary $y=0$ is diffusely reflecting with a temperature given by $T_B = T_0(1-\epsilon\cos 2\pi x/L)$; an identical boundary is located at $y=L$ and the Knudsen number based on the separation between the two boundaries L is $Kn=1$.

Due to the underlying symmetries in the x and y directions, the DSMC simulation domain is usually chosen as $0<x,y<L/2$ [22]. However, due to the high efficiency of the unified scheme, a full domain with $L\times L$ is used in the simulation. Here we show results for two choices of $\epsilon=0.001, 0.05$. The temperature profiles are shown in Fig. 5, where the DSMC solutions included are from [22]. Reasonable agreement has been obtained for these cases between unified and DSMC solutions.

(a) $\epsilon=0.001$ (b) $\epsilon=0.05$
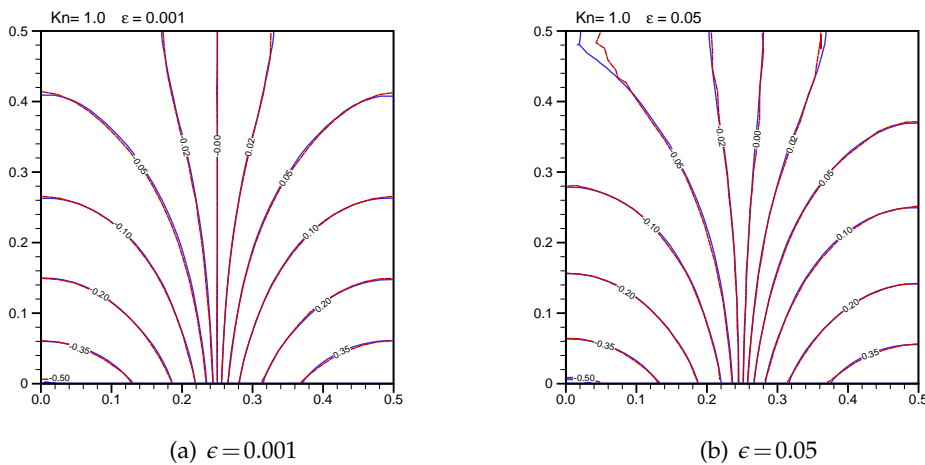
Figure 5: Temperature variations in the thermal creep flow due to nonlinear variation of boundary temperature. Dash-red line: DSMC [22]; solid-blue line: unified scheme.

3.4   Thermal transpiration

This test case follows exactly the cases in Masters and Ye's OSIP-DSMC paper [20]. Consider a system wherein two cavities are maintained at the same initial pressure but dissimilar temperatures and joined by a tube of some length. If the width of the tube is large in comparison to the mean free path of the gas, the Navier-Stokes equations have a uniform pressure solution and a purely diffusion solution for the temperature field without fluid velocity. As the tube becomes narrow, such that the flow goes to transition and free molecular flows, then molecules will creep through the tube from the cold to the hot reservoir. If the reservoirs are sealed, the result will be a static pressure gradient. If they are open, then the result will be a continuous transport or pumping the gas from the cold to the hot reservoir. The detailed explanation can be found in [15, 20]. In the transition regime, the creep flow may eventually be balanced by reverse Poiseuille flow driven by the induced pressure gradient. Many experimental observations of thermal transpiration have been reported [2, 19] as well as practical application of the effect in Knudsen pumps and micropropulsion systems [1, 16, 31]. From a modeling standpoint, a number of different techniques have been proposed, including various solutions of the linearized Boltzmann transport equation [24], near continuum slip models [9, 15] and DSMC simulations [1, 16]. Linearized BTE methods are suitable for problems with small thermal gradients, i.e., weakly non-equilibrium, but are likely inadequate for the complex geometries and large thermal gradients that may be encountered in micro- and nanoscale systems. Near continuum models are only applicable for a small range of flow conditions.

The problem we will first consider in this work is the same cases as presented in [20]. There is a sealed 2D microchannel with a rectangular cross section and geometry suitable for MEMS applications as shown in Fig. 6. The two ends of the channel are maintained at two different temperatures $T1 < T2$ with $T1 = 273K$ and $T2 = 573K$. The temperature of the side walls varies linearly along the surface of the channel and the working argon gas is initially in thermal equilibrium with the walls, i.e., $T(x,y) = (T_2 - T_1)x/L + T_1$ and at a uniform pressure of one atmosphere, i.e., $P(x,y) = P = 1atm$. Therefore, the mean free path of the gas is about $64nm$. The channel is discretized using 200 cells along the length and 40 along the width. Again, the particle velocity space is discretized with 28×28 points for the unified scheme. The wall accommodating coefficient is equal to 1.
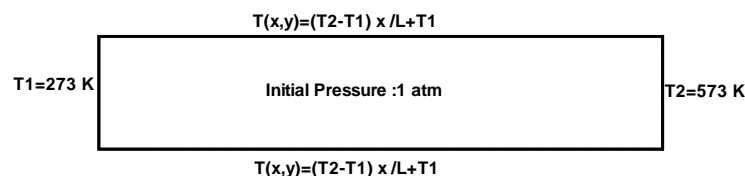
Figure 6: Set-up of thermal creep flow with closed walls. Channel length to width ratio is 5.

(a) channel width $1\mu m$

(b) channel width $100nm$

(c) channel width $20nm$
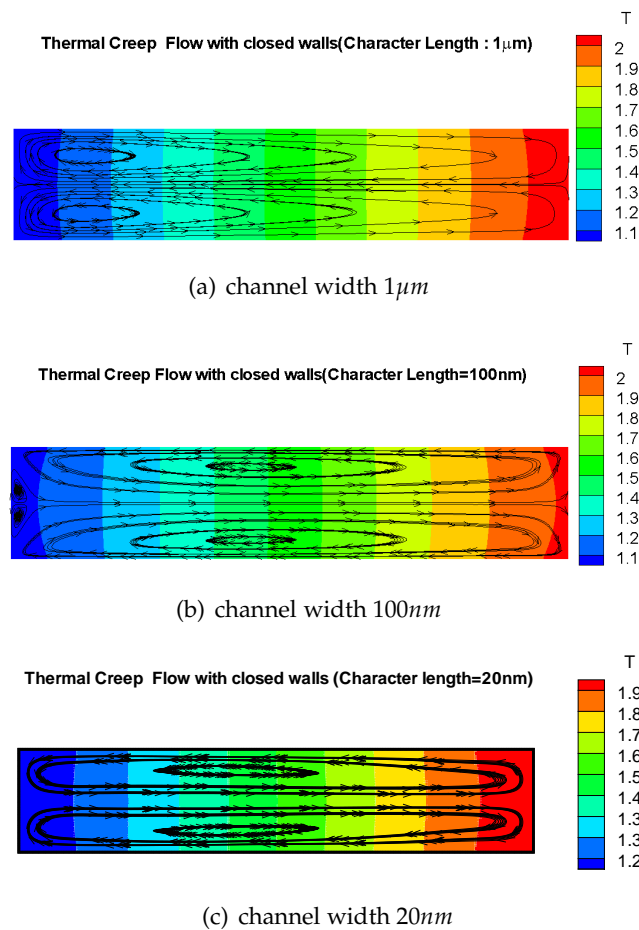
Figure 7: Thermal creep flow with closed walls. Streamline distributions with channel widths $1\mu m$, $100nm$, $20nm$.

Fig. 7 presents streamline distribution inside the tube calculated by the unified scheme at different channel widths $1\mu m$, $100nm$, $20nm$. At $h=1\mu m$, the flow is moving from low temperature region to the high temperature along the boundary and the flow returns in the central region. However, at $h=100nm$, the flow direction is reversed, even though the flow velocity is very small. This phenomena of reversing gas velocity along the wall surface had been observed first by the current unified scheme and later it was confirmed by our intensive DSMC calculation. The obtained pressure distributions along the central line of the tube is shown in Fig. 8 for all three cases. The solutions from the unified scheme match with the DSMC solution very well [20]. Physically, nano-scale confined gas flows are not dynamically similar to the low pressure rarefied gas flows, since the forcing from the wall molecules will effectively cover a significant region of the flow domain [5].
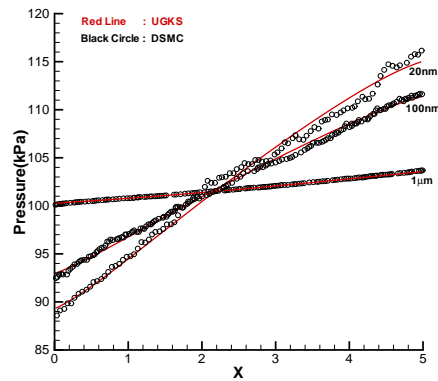
Figure 8: Pressure distribution along the central line of the channel. Circles: DSMC [20], Lines: unified solutions.

At width $h = 1\mu m$, the comparison of temperature and velocity contours between unified and DSMC solutions is shown in Fig. 9, where perfect match has been obtained, especially for the temperature distribution. In order to compare the solution differences between the closed tube and a tube connected with two cavities, we test all three cases of the same tube with widths $1\mu m$, $100nm$, $20nm$, which are connected with two cavities with the same initial pressure and two temperatures T_1 and T_2, see Fig. 10 for set up. Different from the closed tube case, initially the gas will flow from the low temperature cavity to high temperature one. As the pressure piles up inside the high temperature
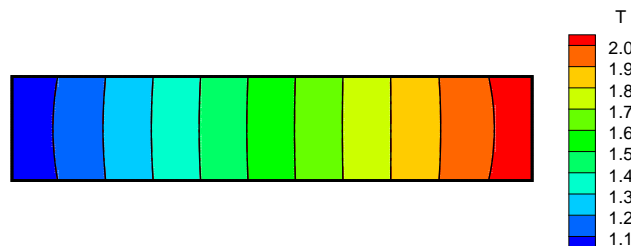
(a) Temperature contours. Solid line: UGKS; dash-dot line: DSMC.
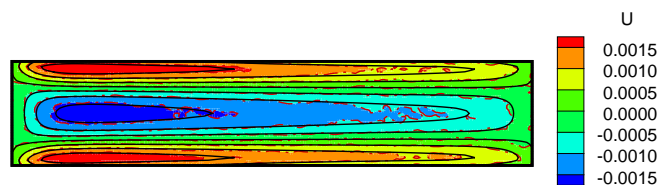
(b) Velocity contours. Solid line: UGKS; dash-dot line: DSMC.

Figure 9: Temperature and velocity contours for the thermal creep flow at channel width $1\mu m$ calculated by unified and DSMC method.
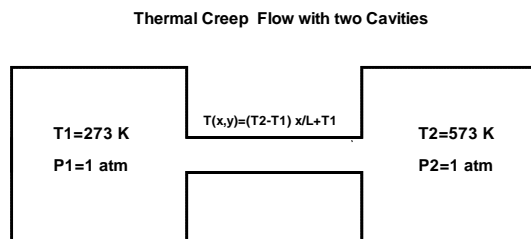
Figure 10: Micro-channel connected with two cavities.

cavity, a back-flow will be formed inside the tube. To the steady state solution, the final mass flux through the tube will be zero, but the pressure gradient is kept along the tube. Fig. 11 shows the streamlines for all three cases. The pressure distributions in these cases
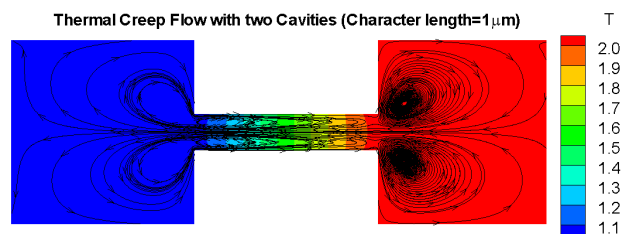
(a) channel width $1\mu m$
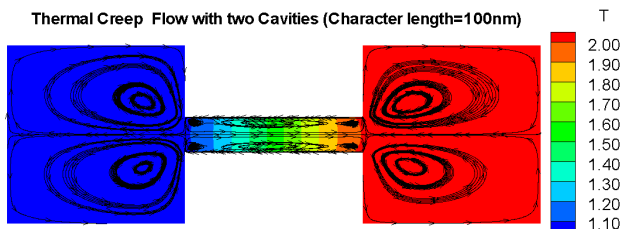
(b) channel width $100nm$
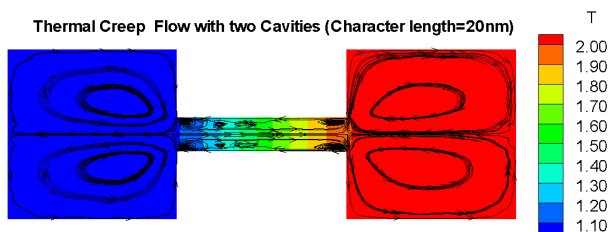
(c) channel width $20nm$

Figure 11: Streamlines for the thermal creep flow with cavities.

(a) channel width $1\mu m$

(b) channel width $100nm$

(c) channel width $20nm$
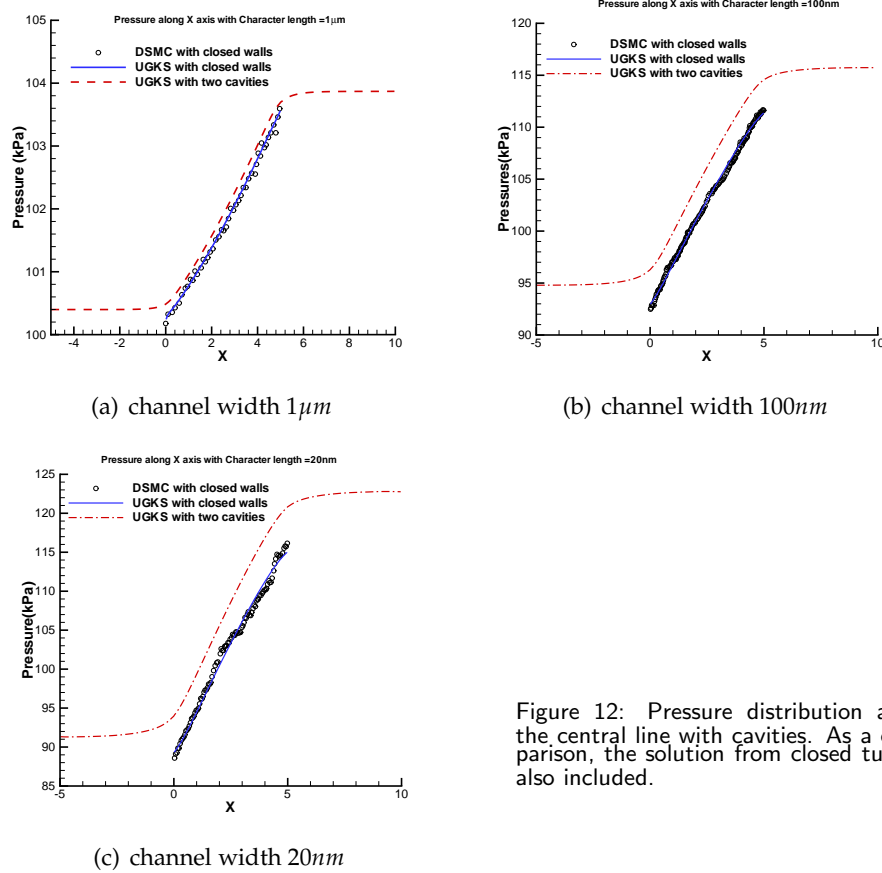
Figure 12: Pressure distribution along the central line with cavities. As a comparison, the solution from closed tube is also included.

are compared with the pressure distribution with closed tube in Fig. 12. As shown in these figures, with the inclusion of two cavities the whole pressure curves are shifted up, but similar pressure differences are kept.

3.5 Flows arising from temperature discontinuities

This case is from the paper by Masters and Ye [20]. In a sealed 2D domain, there is temperature discontinuities at the boundaries. Here we consider two cases with different temperature discontinuous distributions. The schematic of the boundary temperature distribution is shown in Fig. 13.

Case 3.1. The first case was described by Aoki et al.. It consists of a $1\mu m$ square domain with the right and left halves of the boundary assigned different temperatures ($T1=200K$ and $T2=400K$) such that temperature discontinuities are located at the midpoints of the upper and lower boundaries [4], Fig. 13(a). The unified scheme is applied to this problem: discretizing the lower half of the domain with 40×20 mesh points in the physical space and 28×28 mesh points in the velocity space. Fig. 14 shows the velocity field distribution

(a) Case 3.1   (b) Case 3.2
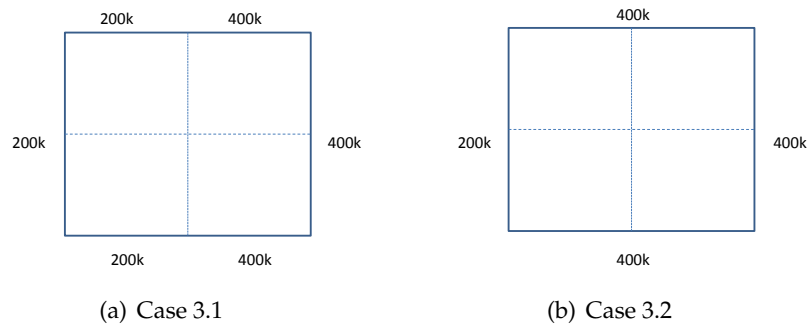
Figure 13: Two schematic cases with discontinuous temperature.

obtained from Boltzmann solution in [4]. The velocity arrows in this figure point out an interesting phenomena, where the velocity vectors suddenly change the direction along the boundary. It seems that there is a sink and source on the boundary. The IP-DSMC solutions in [20] do not clearly show this phenomena. Fig. 15 presents the streamlines obtained from the unified simulation. In comparison with the DSMC and linearized Boltzmann solution in [20], much detailed flow structure has been obtained using the unified scheme. The source and sink at the boundary in the Boltzmann solution are coming from two weak vortices around the corners.
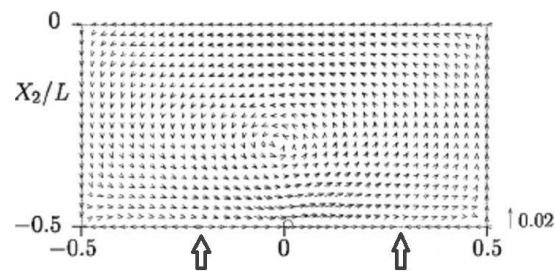
Figure 14: Case 3.1 test at $Kn=0.2$ and $T_L=200K$, $T_R=400K$. Results for the half domain from the kinetic solution of Aoki, et al. [4]. The arrows point to the locations where the velocity vectors change direction at the boundary.
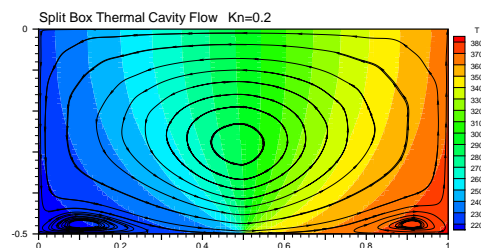
Figure 15: Case 3.1 test at $Kn=0.2$ and $T_L=200K$, $T_R=400K$: unified scheme streamlines. There are two small vortices around the lower left and right corners, which explain the velocity direction reverse in Fig. 14 along the boundary.

Case 3.2. The next example again consists of a $1\mu m$ square domain, with one side maintained at $T1=200K$ and other three sides at $T2=400K$, see Fig. 13(b). For unified scheme, the whole physical domain are covered by 80×80 mesh points and the velocity space has 28×28 mesh points. The initial uniform pressure of inside the domain is $1atm$, which corresponds to $Kn=0.1$. The results of the unified scheme and DSMC solutions are presented in Figs. 16 for the velocity vector field in Fig. 16(a), streamline in Fig. 16(b) and temperature distributions in Fig. 16(c). Reasonable agreements have been obtained between these two solutions. The above DSMC solution is obtained using the original DSMC method without IP technique. The streamline in the above solution seems different from the OSIP-DSMC result in [20].

(a) Up: Unified, Down: DSMC

(b) Up: Unified, Down: DSMC

(c) Up: Unified, Down: DSMC
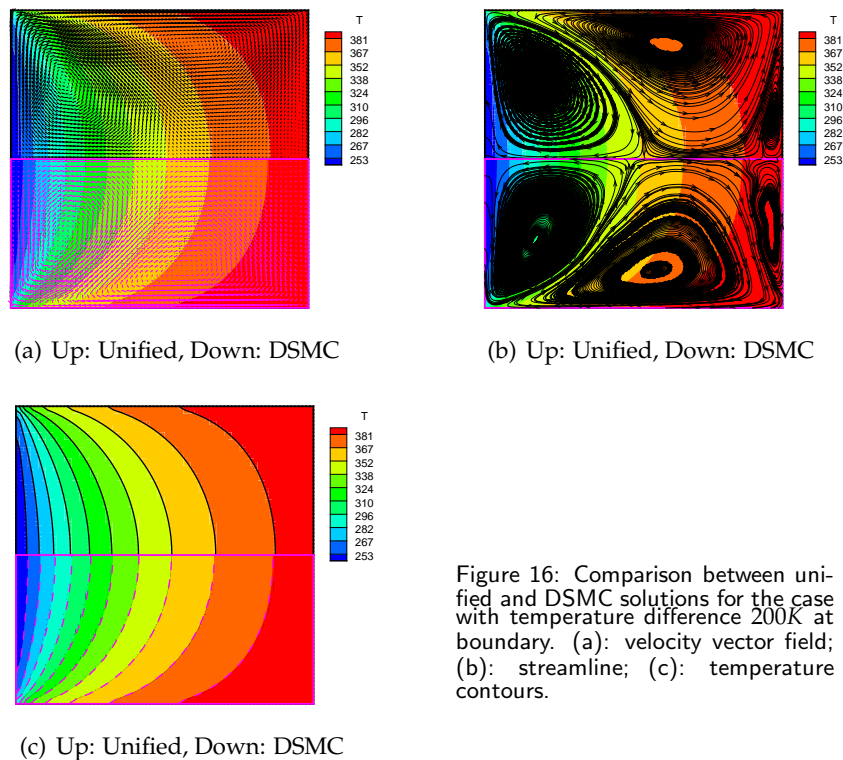
Figure 16: Comparison between unified and DSMC solutions for the case with temperature difference $200K$ at boundary. (a): velocity vector field; (b): streamline; (c): temperature contours.

Convergence study

In order to validate the unified scheme further, we conducted the convergence study with different mesh points in physical and velocity space. For the above Case 3.2, the converged temperature contours with physical space mesh points, i.e., 40×40, 60×60 and 80×80 and velocity mesh points, i.e., 20×20, 25×25 and 28×28, are shown in Fig. 17. Identical results can be obtained by the unified scheme with a variation of the mesh points in both physical and velocity space.

(a) velocity space 20×20

(b) velocity space 25×25

(c) velocity space 28×28
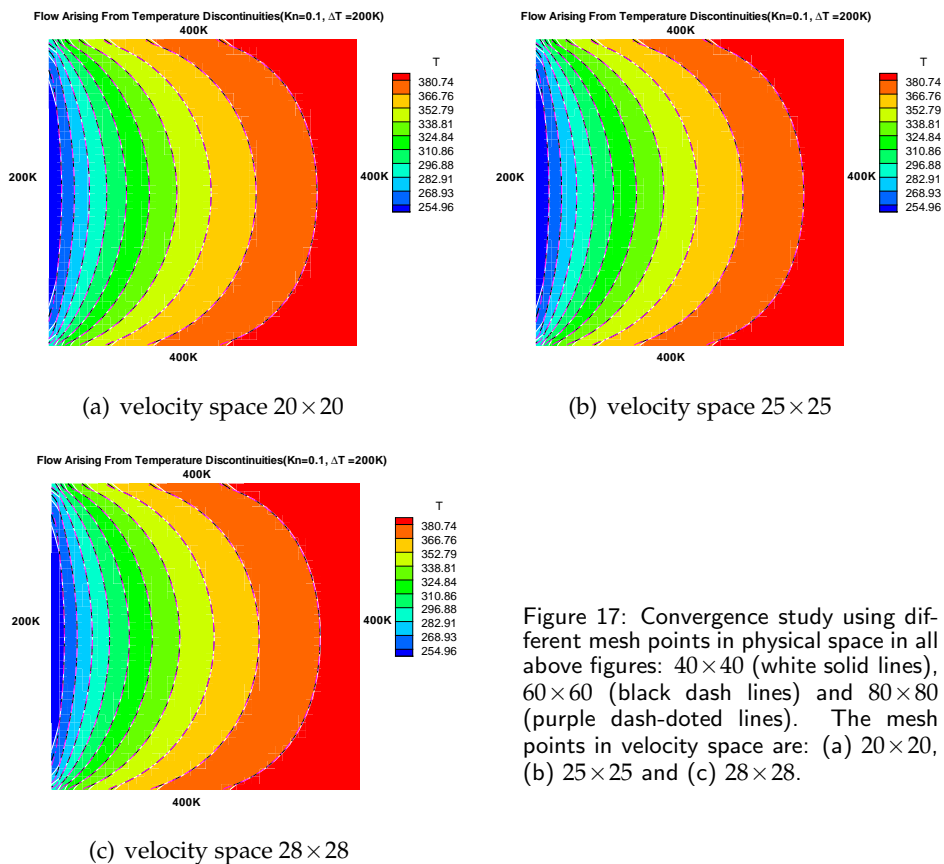
Figure 17: Convergence study using different mesh points in physical space in all above figures: 40×40 (white solid lines), 60×60 (black dash lines) and 80×80 (purple dash-doted lines). The mesh points in velocity space are: (a) 20×20, (b) 25×25 and (c) 28×28.

In order to further test the sensitivity of the unified scheme to the temperature differences in the above Case 3.2, we reduce the temperature difference from $200K$ to $2K$. With different temperature differences, the converged flow patterns are shown in Fig. 18. With the same physical space mesh points 80×80, Fig. 18 presents the results with different mesh points in the velocity space, i.e., 20×20, 25×25 and 28×28. Since the x and y direction fluid velocities are relatively sensitive variables, Fig. 18 basically confirms the accuracy of the unified scheme with 28×28 mesh points in the low speed microflows. It is also interesting to see the velocity magnitude generated by the temperature differences at $Kn=0.1$. With $\Delta T=200K$, the maximum velocity can reach $0.5m/s$, but it goes to around $0.01m/s$ for $\Delta T=2K$.

Efficiency study

In order to show the speed of the unified scheme to get to the converged solution and the computational efficiency, in the above test cases with temperature differences of $200K$ and $2K$, we define a maximum error at each computational step using the data from the

(a) Temperature distribution

(b) Temperature distribution

(c) *x*-component velocity contour

(d) *x*-component velocity contour

(e) *y*-component velocity contour

(f) *y*-component velocity contour
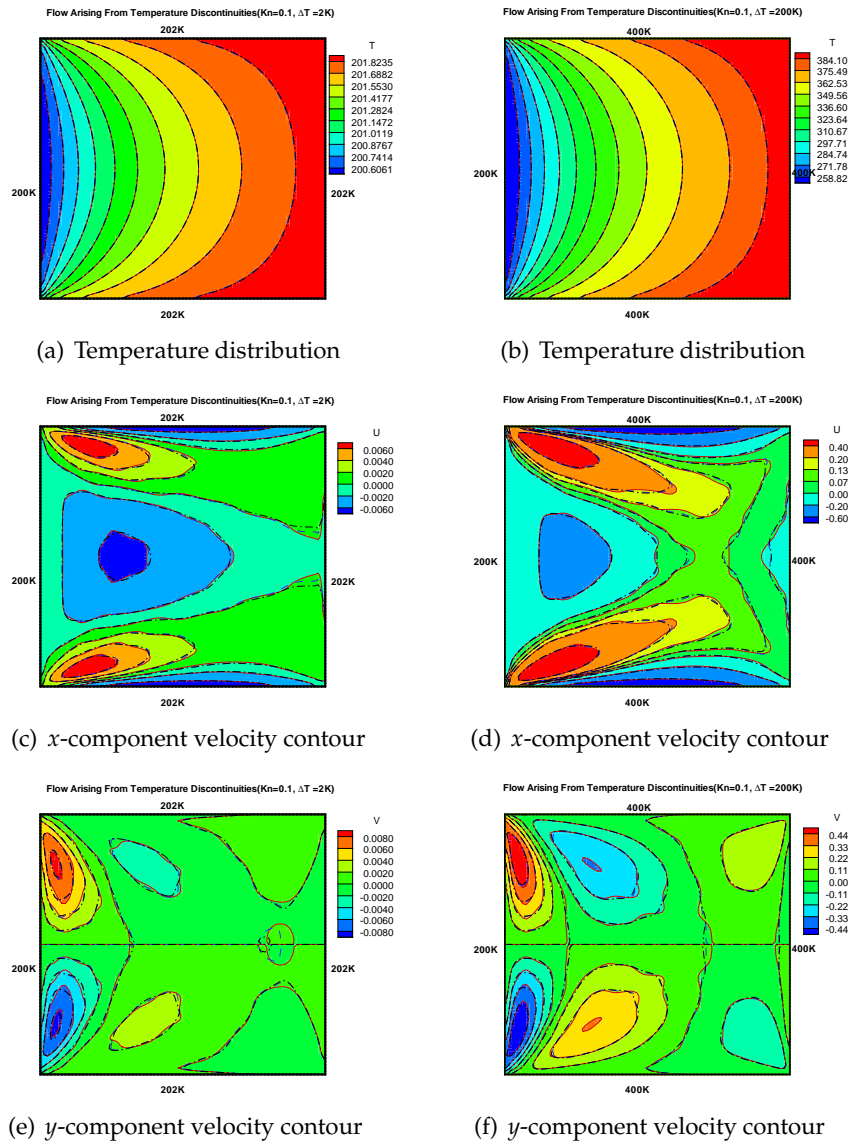
Figure 18: Convergence study for different temperature differences. The physical space mesh points is fixed by 80×80. Left columns: $\Delta T = 2K$. Right Columns: $\Delta T = 200K$. With fixed mesh points in the physical space, mesh points in velocity space in all above figures are 20×20 (red solid line), 25×25 (blue dashed line), 28×28 (black dash-dotted line).

explicit unified scheme,

$$\epsilon_n = \text{Max}_{i,j}\left(|\rho^{n+1} - \rho^n|, |(\rho U)^{n+1} - (\rho U)^n|, |(\rho V)^{n+1} - (\rho V)^n|, |(\rho E)^{n+1} - (\rho E)^n| \right),$$

in the whole physical domain and use the condition $\epsilon_n \leq 10^{-7}$ for convergence. The following Table 1 presents the mesh points, temperature difference, total steps for conver-

Table 1: Maximum error $\epsilon \leq 10^{-7}$ based on machine: Intel (R) Core TM I5-2500, CPU @ 3.30GHz 3.30GHz.

Physical space	Velocity space	ΔT	Total steps	CPU time (min)
80×80	28×28	200	5667	40.2
80×80	25×25	200	5667	39.5
80×80	20×20	200	6661	22.5
60×60	28×28	200	5159	18.0
60×60	25×25	200	5159	17.8
60×60	20×20	200	5159	9.8
40×40	28×28	200	3703	5.9
40×40	25×25	200	3703	5.7
40×40	20×20	200	3703	4.2
80×80	28×28	2	3148	19.2
80×80	25×25	2	3148	18.8
80×80	20×20	2	3148	10.5
60×60	28×28	2	2775	9.5
60×60	25×25	2	2775	9.4
60×60	20×20	2	2775	5.2
40×40	28×28	2	1466	2.4
40×40	25×25	2	1585	2.3
40×40	20×20	2	1485	1.2

gence and total CPU time for the machine Intel (R) Core TM I5-2500, CPU3.3GHz, which is used in our calculations. Since it is very hard to compare the efficiency for different schemes using different machines and different style of programming, the above table gives a good reference for others to figure out the relative speed of the unified scheme in comparison with their in-house codes.

At end, Fig. 19 presents the error changes with the computational time steps for the
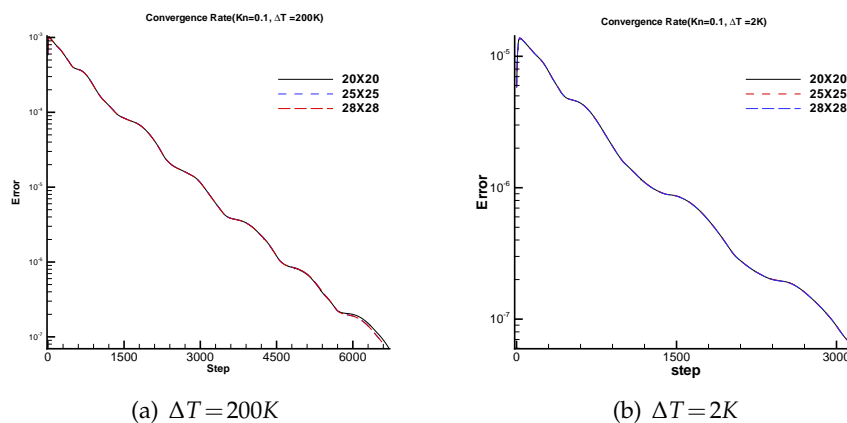
(a) $\Delta T = 200K$ (b) $\Delta T = 2K$

Figure 19: Convergence history with fixed physical space mesh (80×80) and different mesh points in velocity space, i.e., 20×20, 25×25 and 28×28. (a) $\Delta T = 200K$, (b) $\Delta T = 2K$. With lower temperature difference, the convergence is faster.

above simulation using unified scheme and different mesh points in the velocity space. As shown in this figure, the same error reducing for each step with different velocity mesh points is observed. Also, an interesting phenomena for the unified scheme is that as the temperature difference becomes smaller, the unified scheme gets the steady state faster. This property is different from the DSMC method for microflow simulations.

4   Discussion and conclusions

In this paper, a unified scheme has been applied to microflow simulations. The numerical examples cover a whole range of flow regimes from free molecular to the continuum one. The capacity of the unified scheme in capturing non-equilibrium flow behavior has been fully explored in this study. The success of the current method is mainly due to the use of the integral solution of the kinetic model for the evaluation of interface fluxes. Instead of solving the collisionless Boltzmann equation for the particle transport, the full physics of particle movement, i.e., free transport and collision, has been included in the interface flux modeling. As a result, both hydrodynamic and kinetic scale physics has been naturally merged into the time evolution of a single gas distribution function at the cell interface. In the transition flow regime, both scale physics contributes to the flow evolution and to the capturing of non-equilibrium flow behavior. In comparison with the particle-based DSMC method, there is no statistical scattering in the unified solution and the non-equilibrium flow motion due to the small temperature variation can be fully identified. For the low speed microflow, the non-equilibrium effect can be captured reasonably using a limited number of grid points. The efficiency of the unified scheme has been demonstrated as well.

The merit of the unified scheme is in the modeling of interface flux. If the collisionless Boltzmann equation is used for the flow transport at a cell interface, even with the same strategy of updating both macroscopic flow variables and microscopic gas distribution function, in the near continuum flow regime where the cell size is much larger than the particle mean free path, the updated macroscopic variables would not be accurate enough to recover the NS solution, because the collisionless mechanism introduces a cell size proportional numerical dissipation which can become much larger than the physical one. In conclusion, the unified scheme is a useful method for low speed microflow study, especially for the cases with the co-existing of continuum and rarefied flow regimes and with small temperature variations.

Acknowledgments

References

 [1] A. A. Alexeenko, S. F. Gimelshein, E. P. Muntz and A. D. Ketsdever, Modeling of thermal transpiration flows for Knudsen compressor optimization meeting, in: Presented at 43rd Aerospace Sciences Meeting, Reno, NV, AIAA Paper 2005-963 (2005).
 [2] B. K. Annis, Thermal creep in gases, J. Chem. Phys., 57 (1972), 2898–2905.
 [3] K. Aoki, S. Takata, A. Hidefumi and F. Golse, A rarefied gas flow caused by a discontinuous wall temperature, Phys. Fluids, 13 (2001), 2645–2661.
 [4] Kazuo Aoki, Pierre Degond and Luc Mieussens, Numerical simulations of rarefied gases in curved channels: thermal creep, circulating flow and pumping effect, Commun. Comput. Phys., 6(5), 919–954.
 [5] Murat Barisik and Ali Beskok, Molecular dynamics simulations of shear-driven gas flows in nano-channels, Microfluid Nanofluid, 11 (2011), 611–622.
 [6] O. M. Belotserkovskii and Y. I. Khlopkov, Monte Carlo Methods in Mechanics of Fluid and Gas, World Scientific, 2010.
 [7] Alfred E. Beylich, Solving the kinetic equation for all Knudsen numbers, Phys. Fluids, 12 (2000), 444.
 [8] P. L. Bhatnagar, E. P. Gross and M. Krook, A Model for collision processes in gases I: small amplitude processes in charged and neutral one-component systems, Phys. Rev., 94 (1954), 511–525.
 [9] J. R. Bielenberg and H. Brenner, A continuum model of thermal transpiration, J. Fluid Mech., 546 (2006), 123.
[10] G. A. Bird, Molecular Gas Dynamics and the Direct Simulation of Gas Flows, Oxford Science Publications, 1994.
[11] J. M. Burt and I. D. Boyd, Convergence detection in direct simulation Monte Carlo calculations for steady state flows, Commun. Comput. Phys., 10 (2011), 807–822.
[12] S. Chapman and T. G. Cowling, The Mathematical Theory of Non-Uniform Gases, Cambridge University Press, 1990.
[13] S. Z. Chen, K. Xu, C. B. Li and Q. D. Cai, A unified gas kinetic scheme with moving mesh and velocity space adaptation, J. Comput. Phys., 231 (20) (2012), 6643–6664.
[14] J. Fan and C. Shen, Statistical simulation of low-speed rarefied gas flows, J. Comput. Phys., 167 (2001), 393–412.
[15] G. Karniadakis, A. Beskok and N. Aluru, Microflows and Nanoflows, Springer Science+Business Media, Inc., 2005.
[16] Y. L. Han, Working gas temperature and pressure change for microscale thermal creep-driven flow caused by discontinuous wall temperature, Fluid Dyn. Res., 42 (2010), 1–23.
[17] J. C. Huang, K. Xu and P. B. Yu, A unified gas-kinetic scheme for continuum and rarefied flows II: multidimensional cases, Commun. Comput. Phys., 3(3) (2012), 662–690.
[18] M. N. Kogan, Rarefied Gas Dynamics, Plenum Press, New York, 1969.
[19] M. Knudsen, The Kinetic Theory of Gases, third ed., Wiley, New York, 1950.
[20] N. D. Masters and W. Ye, Octant flux splitting information preserving DSMC method for thermally driven flows, J. Comput. Phys., 226 (2007), 2044–2062.
[21] Koji Morinishi, Numerical simulation for gas microflows using Boltzmann equation, Comput. Fluids, 35 (2006), 978–985.

[22] G. A. Radtke, N. G. Hadjiconstantinou and W. Wagner, Low-noise Monte Carlo simulation of the variable hard sphere gas, Phys. Fluids, 23 (2011), 030606.
[23] E. M. Shakhov, Generalization of the Krook kinetic equation, Fluid Dyn., 3(1968), 95.
[24] F. Sharipov, Non-isothermal gas flow through rectangular microchannels, J. Micromech. Microeng., 9 (1999), 394–401.
[25] Y. Sone, S. Takata and T. Ohwada, Numerical analysis of the plane Couette flow of a rarefied gas on the basis of the linearized Boltzmann equation for hard-sphere molecules, Euro. J. Mech. B/Fluids, 9 (1990), 273.
[26] Q. Sun and I. D. Boyd, A direct simulation method for subsonic microscale gas flows, J. Comput. Phys., 179 (2002), 400–425.
[27] Q. Sun, Information Preservation Methods for Modeling Micro-Scale Gas Flows, Ph.D. thesis, 2003, The University of Michigan.
[28] F. G. Tcheremissine, Solution of the Boltzmann kinetic equation for low speed flows, Transport Theory Statistical Phys., 37 (2008), 564–575.
[29] V. A. Titarev, Implicit unstructured-mesh method for calculating Poiseuille flows of rarefied gas, Commun. Comput. Phys., 8 (2010), 427–444.
[30] V. A. Titarev, Efficient deterministic modelling of three-dimensional rarefied gas flows, Commun. Comput. Phys., 12 (2012), 162–192.
[31] S. E. Vargo, E. P. Muntz, G. R. Shiflett and W. C. Tang, Knudsen compressor as a micro- and macroscale vacuum pump without moving parts or fluids, J. Vacuum Sci. Tech. A, 7 (1999), 2308–2313.
[32] R. J. Wang and K. Xu, The study of sound wave propagation in rarefied gases using unified gas-kinetic scheme, Acta Mech. Sinica, 28 (2012), 1022–1029.
[33] K. Xu, Numerical Hydrodynamics from Gas-Kinetic Theory, Ph.D. thesis, 1993, Columbia University.
[34] K. Xu, A Gas-Kinetic BGK scheme for the Navier-Stokes equations and its connection with artificial dissipation and Godunov method, J. Comput. Phys., 171 (2001), 289–335.
[35] K. Xu, Regularization of the Chapman-Enskog expansion and its description of shock structure, Phys. Fluids, 14(4) (2002), L17–L20. DOI: 10.1063/1.1453467
[36] K. Xu and J. C. Huang, A unified gas-kinetic scheme for continuum and rarefied flows J. Comput. Phys., 229 (2010), 7747–7764.
[37] K. Xu and J. C. Huang, An improved unified gas-kinetic scheme and the study of shock structures, IMA J. Appl. Math., 76(5) (2011), 698–711.
[38] K. Xu and E. Josyula, Continuum formulation for non-equilibrium shock structure calculation, Commun. Comput. Phys., 1(3) (2006), 425–448.
[39] K. Xu, H. W. Liu and J. Z. Jiang, Multiple-temperature kinetic model for continuum and near continuum flows, Phys. Fluids, 19 (2007), 016101. DOI: 10.1063/1.2429037.
[40] J. Zhang, J. Fan and J. Z. Jiang, Multiple temperature model for the information preservation method and its application to nonequilibrium gas flows, J. Comput. Phys., 230 (2011), 7250–7256.